6656 *Macromolecules* **2009**, *42*, 6656–6664
DOI: 10.1021/ma900537c

Macromolecules
ARTICLE

Nanograin Evolution in Cold Crystallization of Syndiotactic Polystyrene As Illustrated via in-Situ Small/Wide-Angle X-ray Scattering and Differential Scanning Calorimetry

C. H. Su,[†] U. Jeng,*[,†] S. H. Chen,[‡] S. J. Lin,[‡,§] W. R. Wu,[§] W.-T. Chuang,[†] J. C. Tsai,[⊥] and A. C. Su*[,§]

[†]*National Synchrotron Radiation Research Center, Science-Based Industrial Park, Hsinchu 300, Taiwan,* [‡]*Department of Materials Science and Engineering, National Dong Hwa University, Hualien 974, Taiwan,* [§]*Department of Chemical Engineering, National Tsing Hua University, Hsinchu 300, Taiwan, and* [⊥]*Department of Chemical Engineering, National Chung Cheng University, Chiayi 621, Taiwan*

Received March 12, 2009; Revised Manuscript Received June 8, 2009

Downloaded by SYNCHROTRON RADIATION RES CTR on September 1, 2009 | http://pubs.acs.org
Publication Date (Web): June 25, 2009 | doi: 10.1021/ma900537c

ABSTRACT: Structural evolution of syndiotactic polystyrene (sPS) in a cold crystallization process was quantitatively examined with in-situ small/wide-angle X-ray scattering and differential scanning calorimetry (SAXS/WAXS/DSC). After removal of background scattering from fractal-like matrix structure, SAXS profiles obtained during programmed heating of an amorphous sPS specimen from 30 to 240 at 10 °C/min can be interpreted with a similar sequence of events previously observed in cold crystallization of poly(9,9-di-*n*-octyl-2,7-fluorene) (PFO). Specifically, the nanograin evolution of sPS involves four stages: (1) the frozen-in stage below 90 °C, (2) the nucleation of *oblate*-like nanograins with a constant radius of gyration $R_g \approx 2.6$ nm between 90 and 130 °C, (3) the growth of nanograin size to $R_g \approx 3.2$ nm concomitant with the emergence and development of WAXS-determined crystallinity ($X_{c,WAXS}$) from 130 to 180 °C, and finally (4) the coalescence (and thickening) of the nanocrsytals into a greater size of $R_g \approx 4.6$ nm upon further heating up to 240 °C. Developments in the DSC-determined crystallinity ($X_{c,DSC}$) coincided with nucleation and growth stages, whereas the SAXS-determined heterogeneity (Q_{inv}) increased steadily throughout nucleation, growth, and coalescence stages. Little changes of morphological features in the nanometer-length scale can be observed with subsequent isothermal annealing at 240 °C up to 1 h; the final size of coalesced nanograins at this temperature is therefore attributed to the balance between the tendency to eliminate lateral surface via coalescence and the opposing strain field (due to locked and tightened entanglements) in the surrounding matrix. Delicate differences in nanograin size and shape during cold crystallization processes of sPS and PFO are discussed in terms of differences in chain rigidity (random coiled vs semirigid) and melt structure (isotropic vs nematic).

Introduction

In recent years, increasingly more experimental evidence from microscopic techniques[1−8] have demonstrated that polymer crystal surfaces often comprise nodules in the nanometer-sized scale. Complementary to imaging studies, X-ray and light scattering observations in a number of polymeric materials suggest a precursory ordering process prior to crystallization.[9−19] In previous scattering studies, density fluctuations before crystallization were typically analyzed in terms of correlation function or scattering invariant, which gave only indirect information on morphological features before the formation of stacked crystalline lamellae. With a different approach in SAXS data analysis for the cold crystallization of a conjugated polymer, poly(9,9-di-*n*-octyl-2,7-fluorene) (PFO),[20] we have *quantitatively* correlated structural features revealed via in-situ small/wide-angle X-ray scattering (SAXS/WAXS) to nodules observed in earlier scanning/transmission electron microscopic (SEM/TEM) images. Specifically, using analytical models of prolate/oblate ellipsoids, we have interpreted the observed density fluctuations during cold crystallization of PFO in terms of nucleation, growth, and coalescence of nanograins. Similar evolution of nodular structure was also qualitatively proposed by Konishi et al.[21] for the crystallization of isotactic polypropylene (iPP) upon heating of a quenched mesomorphic glass.

In spite of the fact that PFO of conjugated (and semirigid) backbone with *n*-octyl grafts (providing amphiphilic characteristics in terms of aromatic vs aliphatic interactions) is *not* a typical polymer, we were nevertheless compelled to comment[20] on similarities and differences of the proposed nanograin picture as compared to earlier concepts of nanocrystalline blocks by Perlin,[22] mesomorphic precursor by Strobl,[18] and spinodal-like cold crystallization mechanism by Ryan in particular.[19] For a more realistic comparison, here we report results of our recent investigation on the cold crystallization of a more traditional polymer of random-coil chains, syndiotactic polystyrene (sPS). Using synchrotron-based, in-situ/simultaneous SAXS/WAXS and differential scanning calorimetry (DSC), we illustrate features of nanograin evolution during cold crystallization of sPS. Similarities and (delicate yet intriguing) differences in nanograin size and shape between the two contrasting cases of sPS and PFO are discussed.

Experimental Section

Syndiotactic polystyrene was received from the Grand Pacific Petrochemical, with weight-average molecular mass $M_w = 140$ kDa, polydispersity of 2.4, and high stereoregularity (>98% in [*rr*]

*To whom correspondence should be addressed.

 Published on Web 06/25/2009 © 2009 American Chemical Society

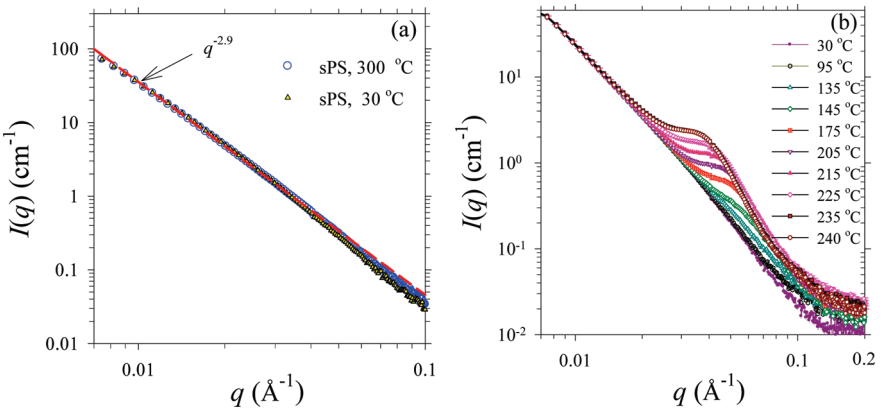

Figure 1. (a) SAXS profiles of the sPS specimen at 30 °C as quench glass and at 300 °C in the melt state. Solid line represents the fitted scaling of $I(q) \sim q^{-2.9}$ (indicated by the arrow). (b) Representative temperature-dependent SAXS profiles obtained during heating from 30 to 240 °C.

Downloaded by SYNCHROTRON RADIATION RES CTR on September 1, 2009 | http://pubs.acs.org
Publication Date (Web): June 25, 2009 | doi: 10.1021/ma900537c

triad content[23] as determined from ^{13}C nuclear magnetic resonance spectroscopy). The sample was purified via precipitation into methanol and consolidated under a protective nitrogen stream at 300 °C before quenching into ice water to give vitrified glass. In-situ SAXS/WAXS/DSC measurements were performed at beamline 17B3 of the National Synchrotron Radiation Research Center (NSRRC).[24] The glassy sPS specimen (ca. 1.0 mm in thickness and 6 mm in diameter) was placed in an aluminum cell of Kapton windows ca. 4 mm in diameter for X-ray incidence. The sample cell was then placed in a modified[20] Mettler Toledo FP84 DSC cell holder for simultaneous SAXS/WAXS/DSC measurements.

With an 8 keV (wavelength $\lambda = 1.55$ Å) beam (ca. 0.5 mm in diameter), SAXS, WAXS, and DSC data were simultaneously collected during heating (at 10 °C/min) of specimen from 30 to 240 °C and the subsequent isothermal annealing at 240 °C up to 1 h. The synchronized SAXS and WAXS data collection time was set to 1 frame per 30 s throughout the heating/annealing process. With the direct beam offset from the center of the 2-D detector for a wider SAXS q-range, the optimized geometry of the SAXS/WAXS/DSC setup covered the two main WAXS reflections of sPS α crystals in the q-range of 0.6−1.1 Å^{-1} and a SAXS q-range of 0.007−0.34 Å^{-1}; the corresponding sample-to-detector distances for the 2-D (CCD) SAXS and 1-D (gas-type) WAXS detectors were 1716 and 850 mm, respectively. The scattering wavevector $q \equiv 4\pi\lambda^{-1} \sin\theta$ (with 2θ the scattering angle) was calibrated using silver behenate, sodalite, and silicon powder filled in a cell with 1 mm X-ray path length under the same sPS sample environment. Scattering data were corrected for sample transmission, background, and detector sensitivity. SAXS data were placed in the absolute scale (defined as the differential scattering cross section per unit volume, hence in units of cm^{-1})[25] according to established procedures.[20,24] Experimental reproducibility was generally confirmed by repeated runs using fresh specimens.

To observe detailed molecular ordering during crystallization, in-situ WAXS/DSC, covering most of the Bragg reflections of sPS in a broader q-range of 0.2−2.1 Å^{-1}, was further performed at the powder X-ray diffraction endstation of beamline 01C (16 keV, $\lambda = 0.775$ Å, sample-to-detector distance = 324 mm) at NSRRC. All other experimental parameters were kept unaltered; i.e., the same specimen preparation procedure, the same DSC setup, and the same heating rate, etc., were adopted.

Data Analysis

SAXS intensity profiles were modeled according to $I(q) = I_0 P(q) S(q)$, where $P(q)$ is the normalized form factor of the nanograins (i.e., $P(0) = 1$), $S(q)$ the structure factor, and $I_0 = n_p(\Delta\rho)^2 V^2$ the zero-angle scattering intensity, with nanograin concentration n_p, nanograin volume V, and scattering contrast $\Delta\rho$.[20,25,26] The scattering contrast between the nanograins and the matrix was assumed constant throughout the cold crystallization process. Comparing to spheres, rods, or disks, the ellipsoidal form factor was found to best-fit experimental data. With semimajor axis A and semiminor axis B, the ellipsoid form factor averaged for spatial orientation is given by $P(q) = \int_0^1 |3j_1(\nu)/\nu|^2 \, d\mu$, where $\nu = q[A^2\mu^2 + B^2(1-\mu^2)]^{1/2}$ and j_1 is the spherical Bessel function of the first order.[25,26]

Drawing analogy from micellar solutions, we have adopted the hard-sphere structure factor $S(q) = [1 - n_p C(q)]^{-1}$ to describe spatial arrangement of nanograins, in which $C(q) = 4\pi\sigma^3\xi^{-6}\{\alpha_0\xi^3(\sin\xi - \xi\cos\xi) + \beta_0\xi^2[2\xi\sin\xi - (\xi^2 - 2)\cos\xi - 2] + \gamma[(4\xi^3 - 24\xi)\sin\xi - (\xi^4 - 12\xi + 24)\cos\xi + 24]\}$ with σ the effective diameter, $\xi = q\sigma$, $\alpha_0 = (1+2\phi)^2(1-\phi)^{-4}$ (where ϕ is the effective volume fraction), $\beta_0 = -6\phi[1-(\phi/2)]^2(1-\phi)^{-4}$, and $\gamma = \phi\alpha_0/2$.[27−29] For a system to reach ordered spatial arrangement (such as the distorted FCC-like structure in macro-ion solutions) of dispersed domains, 2σ approaches the value of center-to-center interparticle distance d ($\approx n_p^{-1/3}$).[28−31] In other words, the corona zone surrounding a micellar particle is *incorporated* in σ. For the present case of sPS cold crystallization, the strain field (due to locked/tightened entanglements) developed around a crystallizing nanograin is envisaged to exert interparticle "repulsion" similar in role to the micellar corona layer.

Electron density heterogeneity was evaluated in terms of the scattering invariant $Q_{inv} = \int_0^\infty I(q) q^2 \, dq$ based on the nanograin-matrix-two-phase picture.[26,32] In practice, the upper and lower limits of the integration were replaced by high-q and low-q bounds of SAXS profiles extrapolated for relative scattering invariant.[32] Such an approximation is appropriate when the experimental q-range covers major changes of the SAXS profiles.

The relative crystallinity $X_{c,DSC}$ was extracted from the DSC trace based on the integrated heat flow up to a temperature T, normalized with respect to the *total* heat flow integrated over the entire DSC trace. The relative crystallinity $X_{c,WAXS}$ was obtained from the integrated intensity over the observed Bragg reflections (after subtraction of the amorphous background), normalized by the intensity integrated over the full WAXS profile.

Results

Background Matrix Scattering. Illustrated in Figure 1a are the coinciding SAXS profiles of the sPS specimen obtained either at 300 °C as a melt or at room temperature as a liquid-nitrogen-quenched (from 300 °C) glass; even at 320 °C, ca. 14 °C above the equilibrium melting temperature of the high-melting β phase of sPS,[33] the SAXS profile remains the same. These results indicate the presence of residual

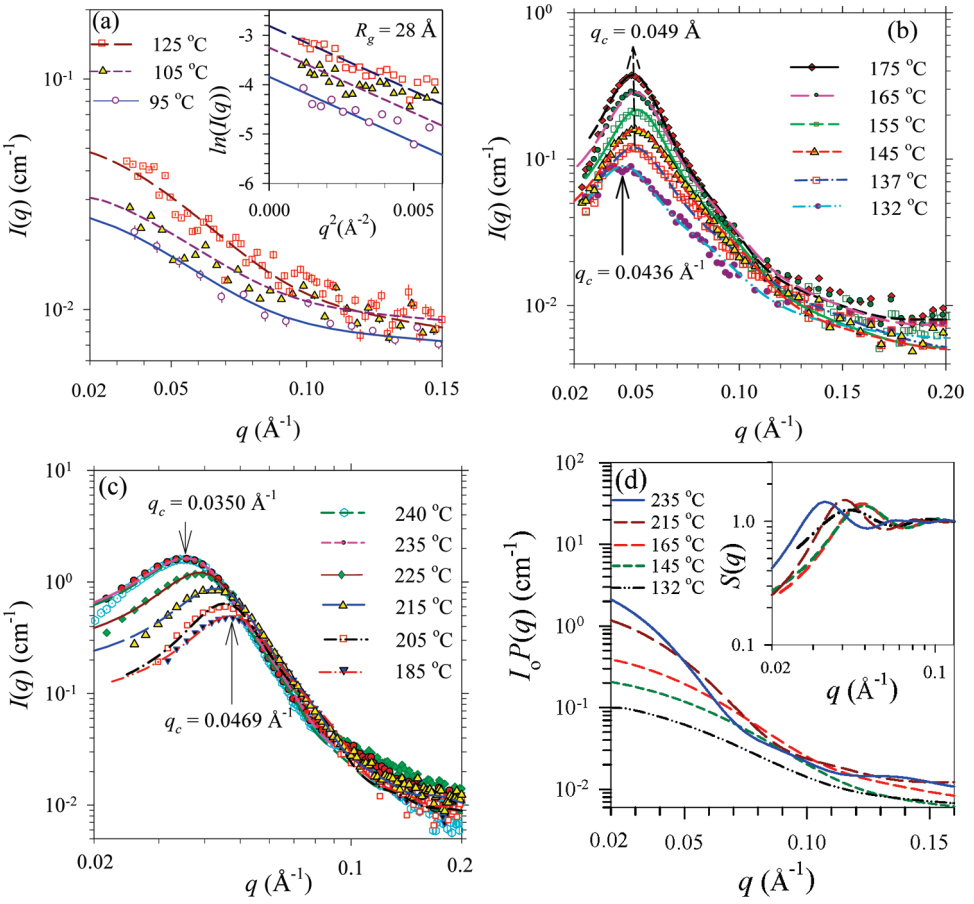

Figure 2. (a) Reduced SAXS profiles obtained at 95, 105, and 125 °C, respectively, fitted with the ellipsoidal form factor. Inset shows the corresponding Guinier plots with a common R_g value of 2.8 nm. (b) SAXS profiles obtained at 132−175 °C and (c) those at 185−240 °C fitted using the ellipsoidal form factor and a hard-sphere structure factor $S(q)$. (d) Representative $I_0P(q)$ and $S(q)$ (inset) curves from the model fitting, with σ=12.8, 11.4, 11.7, 14.0, and 16.4 nm from 132 to 235 °C. This effective diameter includes the strained zone surrounding a nanograin upon crystallization; hence, it is characteristically greater than the oblate minor axis $2B$ and approaches the value of center-to-center interparticle distance d upon full development of distorted FCC-like packing.

nanometer-scale heterogeneity in the melt state that can hardly be removed. The origin of such inhomogeneity is not yet clear; nevertheless, the fractal-like nanostructure of the sPS melt, as revealed by the power-law scattering of $I(q) \sim q^p$ with $p = -2.9 \pm 0.1$ for $q \leq 0.05$ Å^{-1}, can be well frozen and preserved into the glassy state upon quenching. For a mass fractal object composed of primary particles arranged in a self-similar manner,[34−37] the mass increases with linear dimension r in the form of $M(r) \sim r^{D_f}$ whereas the scattering intensity scales as $I(q) \sim q^{-D_f}$. The exponent D_f of a fractal system can be a noninteger between 1 and the Euclidean dimension D. For instance, $D_f = 2$ for Gaussian chains whereas $2 < D_f < 3$ for silica aggregates of porous structure.[34−37] In comparison, conjugated polymers such as PFO or poly(2-methoxy-5-(2′-ethylhexyloxy)-1,4-phenylenevinylene) (MEH−PPV) with nematic order in solution-cast films exhibit power-law scattering with $p \approx -3.4$ as detailed in our previous studies,[4−8,20] which corresponds to surface-fractal structure[34−37] (of a surface fractal dimension of $D_s = 6+p$) with nonsmooth domain−matrix interface.

Shown in Figure 1b are the temperature-dependent SAXS profiles of the sPS specimen obtained during heating from 30 to 240 °C. As temperature was raised to the vicinity of the glass transition temperature T_g (≈95 °C) of sPS, additional scattering (other than that contributed by the glassy matrix) emerged in the higher q region (0.02−0.2 Å^{-1}). This additional scattering develops with increasing temperature up to 240 °C but changes little in the subsequent 1 h annealing at 240 °C, indicating that the kinetic process involved is quickly completed in the time scale of 1 min or so. All SAXS profiles shown in Figure 1b contain a common contribution from the glassy state (i.e., the power-law scattering in Figure 1a). Removal of this constant scattering of the glassy state from the as-obtained SAXS profiles gives the scattering contribution directly related to the structural evolution of sPS nanograins. As detailed below, the reduced SAXS profiles clearly reveal features of nucleation, growth, and coalescence of nanograins.

Nucleation. Illustrated in Figure 2a are SAXS profiles obtained at 95, 105, and 125 °C with the contribution from the glassy matrix subtracted. On the basis of the Guinier approximation[26] (inset of Figure 2a), a common value for the radius of gyration $R_g = 2.8 \pm 0.2$ nm of nanograins can be extracted from the three sets of data. To determine the shape of the nanograins, we fitted the SAXS profiles with possible form factors of spheres, disks, rods, and ellipsoids. Among them, the ellipsoidal form factor gives the best fit; the disk form provides comparable quality of fitting for the same set of data but is consistently higher in terms of χ^2 per degree of freedom (cf. the Supporting Information). The fitted sizes with the disk and ellipsoid shapes for the same set of SAXS data are also comparable; specifically, the oblate shape ($2A \ll 2B$) resembles the disk one, as the values of the major and minor axes $2A$ and $2B$ approach the disk thickness (t) and lateral size ($2r$), respectively. Bearing in mind that the two models provide only approximate shapes of the

Downloaded by SYNCHROTRON RADIATION RES CTR on September 1, 2009 | http://pubs.acs.org
Publication Date (Web): June 25, 2009 | doi: 10.1021/ma900537c

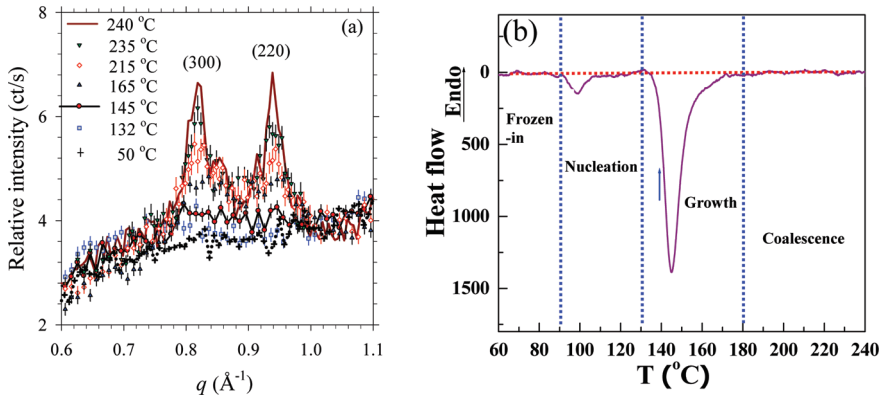

Figure 3. (a) Representative in-situ WAXS profiles (simultaneously obtained with the SAXS profiles in Figure 2) during heating from 30 to 240 °C. (b) The corresponding DSC trace, with the three characteristic temperatures T_1 (≈90 °C), T_2 (≈130 °C), and T_3 (≈180 °C) marked as vertical lines.

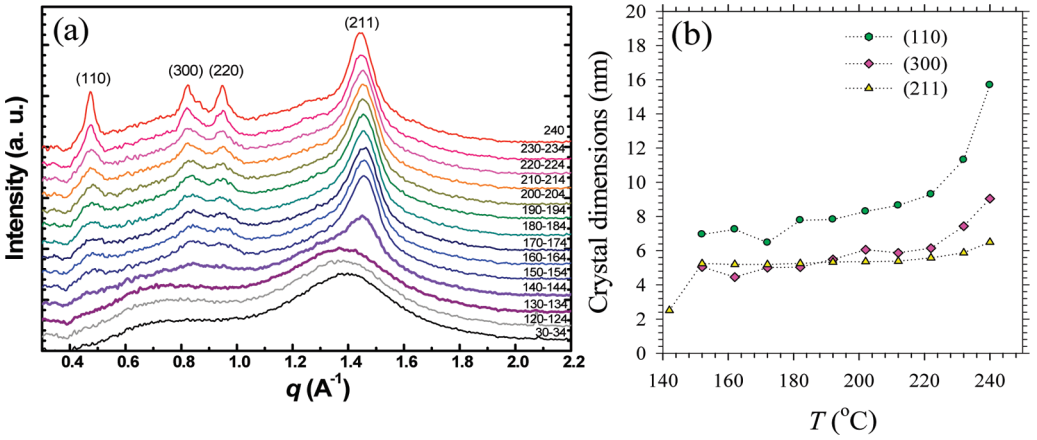

Figure 4. (a) In-situ WAXS spectra of the sPS specimen measured with a powder X-ray diffractometer during the same heating process from 30 to 240 °C as that in the simultaneous SAXS/WAXS/DSC measurements (Figures 2 and 3). Note the emergence of crystalline peaks, especially the (211) reflection above T_2 (≈140 °C), and the gradually sharpened (hk0) reflections above T_3 (≈180 °C). (b) Crystallite dimensions calculated from the peak widths using the Scherrer equation.

nanograins, we consider them equivalent; strict differentiation between the two is artificial.

Shown in Figure 2a are the correspondingly fitted profiles for the nearly constant geometrical features of semimajor axis $A = 1.3 \pm 0.2$ nm and semiminor axis $B = 4.0 \pm 0.2$ nm but different I_0 values of 0.024, 0.035, and 0.042 cm^{-1}, hence increasing nanograin concentrations n_p (proportional to I_0) for the three respective sets of data from 95 to 125 °C. Calculated as[26] $R_g = [(A^2 + 2B^2)/5)]^{1/2}$, the corresponding radius of gyration is 2.6 ± 0.1 nm, consistent with that (2.8 nm) obtained from the model-independent Guinier approximation. The fact that the Guinier approximation (lines in the inset of Figure 2a) can fit relatively well the SAXS data in the nucleation stage with a single slope (i.e., one mean R_g value) implies at most a moderate size distribution;[26,38,39] in the limit of widely distributed particle size, such linearity would be destroyed. (We have attempted to incorporate polydispersity effects in the form of Schultz distribution[38] in the principal axes A and B, but the increased number of fitting parameters rendered the fitting impractical.)

Consequently, the SAXS profiles in Figure 2a (that are well represented by a fixed set of shape/size parameters) are taken to indicate the formation of nanograins above $T_1 \approx$ 90 °C, followed by a nearly 2-fold increase in n_p from 95 to 125 °C. Because of poorly developed long-range positional order within the small nuclei, the nucleation of sPS resulted in no discernible peaks in the concomitant WAXS profiles at or below 132 °C (Figure 3a), which remain essentially unchanged within this temperature range of mainly nucleation. Density within the nucleus, however, must be rather close to crystal density to give adequate contrast for the clearly observable changes in the SAXS profiles; such densification in packing or mesomorphic ordering before development of long-range order contributes to the first exotherm (mainly between 90 and 110 °C and hints of tailing up to 130 °C) in the simultaneously measured DSC profile in this region (Figure 3b).

The mismatch in the broader temperature range of steadily increasing nuclear density and the narrower range of the main exothermic responses at comparatively lower temperatures is intriguing. It may be taken to imply that intermolecular interactions are established first as precursory embryos, releasing a major portion of the corresponding crystallization heat. This is followed by further adjustments in molecular packing and hence densification, yet releasing only residual heat. Shown in Figure 4a are the wide q-range WAXS profiles (separately obtained at the powder X-ray diffractometer end-station at Beamline 01C of NSRRC for a similar sPS specimen) that cover most of the reflections of sPS, including those two monitored WAXS reflections in Figure 3a. The full- range WAXS profiles in Figure 4a indeed support the notion of a frozen-in state below T_g and the general absence of long-range positional order within nuclei up to 132 °C. In other words, the densification in nuclei of limited size is not yet adequate to result in effective diffraction.

Downloaded by SYNCHROTRON RADIATION RES CTR on September 1, 2009 | http://pubs.acs.org
Publication Date (Web): June 25, 2009 | doi: 10.1021/ma900537c

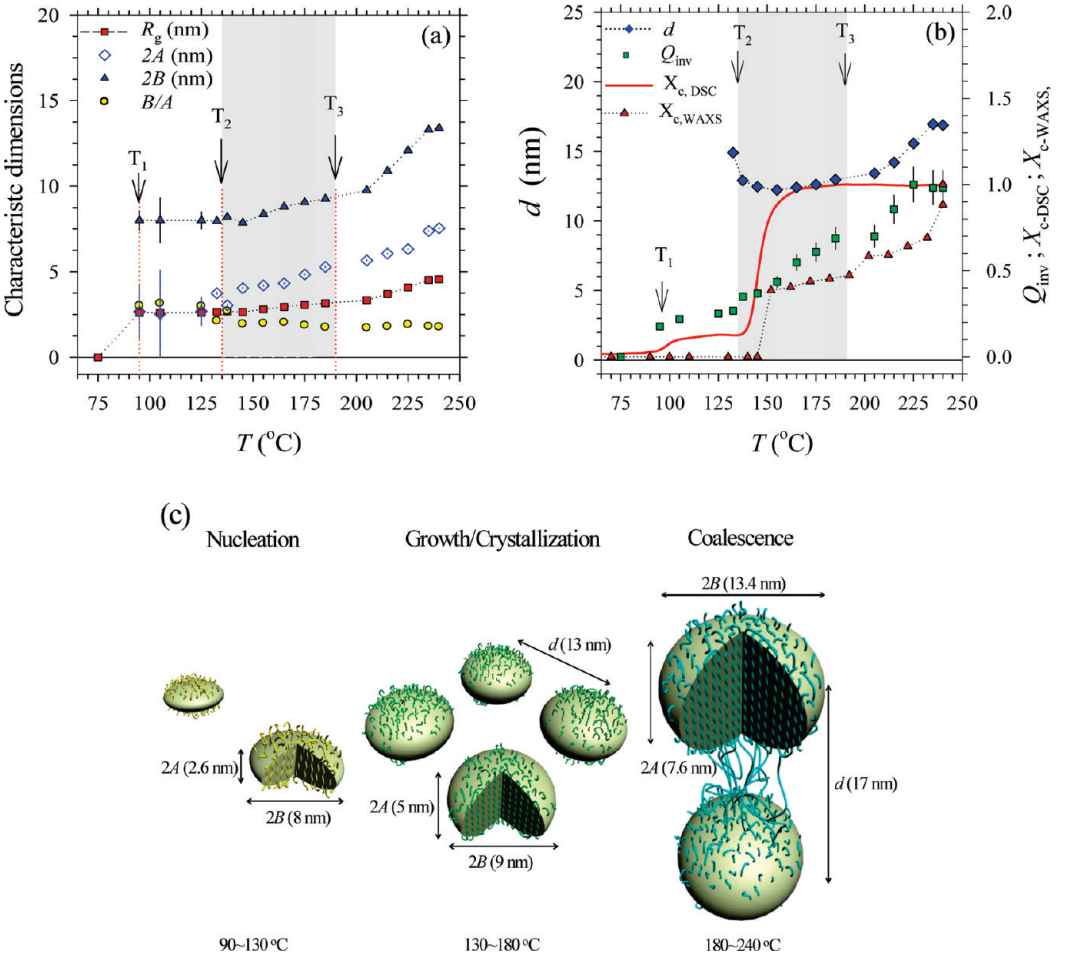

Figure 5. (a) Changes in major axis $2A$ and minor axis $2B$, aspect ratio B/A, and R_g of ellipsoidal nanograins during the programmed heating at 10 °C/min up to 240 °C. (b) Changes in the fitted mean center-to-center intergrain spacing d, the normalized scattering invariant Q_{inv}, and normalized crystallinities extracted respectively from the corresponding DSC trace ($X_{c,DSC}$) and WAXS profiles ($X_{c,WAXS}$). Highlighted are onset temperatures of the nucleation ($T_1 \approx 90$ °C), growth ($T_2 \approx 130$ °C), and coalescence ($T_3 \approx 180$ °C) processes. (c) Cartoons (from left to right) illustrate the structural evolution of sPS nanograins from nucleation (sparsely emerged oblate nuclei), growth/crystallization (ordered nanograins with a mean spacing), to coalescence stages (enlarged oblate nanograins with an increasingly larger spacing).

Growth. As illustrated by the SAXS profiles in Figure 2b, there emerges an interference peak near $q_c = 0.044$ Å^{-1} at 132 °C, which quickly locks into the position of $q_c = 0.049$ Å^{-1} at subsequent temperatures up to 175 °C. Such behavior suggests that, after a quick increase of nanograin concentration n_p up to ca. 130 °C, further heating results in quickly saturated concentration of nuclei $n_p \approx d^{-3}$. The fixed mean center-to-center spacing $d \approx 16$ nm between neighboring nuclei (which corresponds to $n_p \approx 2.3 \times 10^{17}$ nanograins/cm^3) is estimated from $d = 7.884/q_c$ by assuming *distorted* FCC packing of ellipsoids.[31] It should be emphasized that this FCC-like ordering of the nanograins is different from the stacked-lamellae structure in melt-crystallized polymers; hence, the center-to-center intergrain spacing d bears different significance from the long period L in stacked crystalline lamellae.

The scattering invariant (Q_{inv}) increased strongly (by ca. 230%) with a modest decrease in the interference peak width (by ca. 30%), suggesting a growth of the nanograins accompanied by improved intergrain correlation in this temperature range. Nanograin growth is more clearly illustrated by $P(q)$ and $S(q)$ curves (Figure 2d) obtained from model fitting, as to be delineated later. At 145 °C, nanograins with R_g slightly greater than 2.6 nm start to give weak reflections in the corresponding WAXS profile (Figures 3a and 4a), indicating concomitantly improved long-range 3-D crystalline order *within* the growing nanograins. To extract morphological characteristics of concentrated sPS nanograins from SAXS profiles with a prominent interference peak (Figure 2b), we have adopted the Percus−Yevick (PY) hard-sphere $S(q)$, with an effective diameter σ.[28−31,40] This allows for simultaneous resolution of the form factor $P(q)$ and the structure factor $S(q)$, as detailed in the Data Analysis section. Demonstrated in Figure 2b are the SAXS profiles adequately fitted using the equivalent hard-sphere $S(q)$ and $P(q)$ of ellipsoids, with the semimajor and semiminor axes (A, B) growing from (1.5 nm, 4.1 nm) at 132 °C to (2.4 nm, 4.5 nm) at 175 °C; the corresponding R_g value increases from 2.7 to 3.1 nm. Due mainly to the substantial increase in the A value, the *shape anisotropy* of nanograins, represented by the aspect ratio B/A, decreased significantly from 3.0 in the nucleation stage to 1.9 in the growth stage. Fitted parameters are summarized in Figure 5a,b, including the mean center-to-center intergrain spacing d.

Within this growth-dominated temperature range, one may observe (cf. Figures 3a and 4a) emergence of (110), (300), (220), and (211) reflections of α crystals (trigonal in structure, space group $P3$, with a 9-chain unit cell of dimensions $a = b = 2.626$ nm and $c = 0.504$ nm),[41] indicating initial development of long-range positional order upon growth. Concomitantly, the DSC trace in Figure 3b displays the major exothermic event in the form of a prominent second

Downloaded by SYNCHROTRON RADIATION RES CTR on September 1, 2009 | http://pubs.acs.org
Publication Date (Web): June 25, 2009 | doi: 10.1021/ma900537c

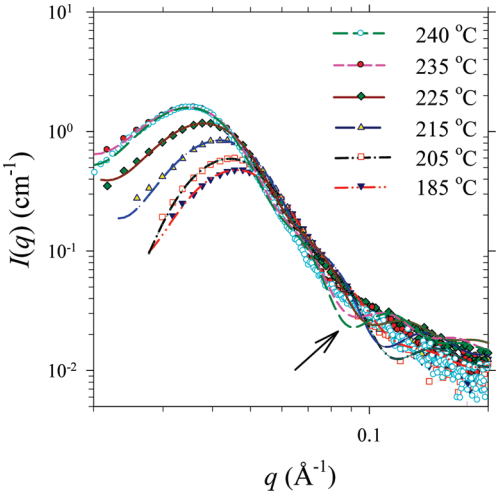

Figure 6. Fitting results of the SAXS data of 185−240 °C (coalescence stage) using the disk form factor and the arrayed lamellar structure factor. The arrow indicates the region where the model fitting curves deviate significantly from the data. Note that much better fitting is obtained in Figure 2c with a combination of the ellipsoid form factor and the equivalent hard-sphere structure factor.

peak between 135 and 160 °C, with clear tailing up to ca. 190 °C. In other words, a minor amount (ca. 10%, Figure 5b) of heat of crystallization is released upon nucleation, with the rest released during the growth stage, leaving no discernible thermal events afterward.

Coalescence. From 185 to 240 °C, SAXS profiles in Figure 2c display a continuous shift of the interference peak from $q_c = 0.047$ to 0.035 Å^{-1} with only a marginal decrease (by 16%) in peak width (from 0.015 to 0.012 Å^{-1}), whereas the peak intensity increases strongly with temperature by more than 3-fold (from 0.5 to 1.8 cm^{-1}). We attribute the growing intensity mainly to size increase, as revealed by the fitted $P(q)$ and $S(q)$ profiles extracted (inset of Figure 2d). Using the same ellipsoidal form factor and hard-sphere structure factor, we fitted respectively SAXS profiles at 185, 205, 215, 225, 235, and 240 °C (Figure 2c) to yield ellipsoid dimensions $(A, B) = (2.6\text{ nm}, 4.6\text{ nm})$, (2.8 nm, 4.9 nm), (3.0 nm, 5.4 nm), (3.2 nm, 6.5 nm), (3.7 nm, 6.7 nm), and (3.8 nm, 6.7 nm), with R_g increasing from 3.2 nm at 185 °C to 4.6 nm at 240 °C and d from 13 to 17 nm. Values of fitted parameters are summarized in Figure 5.

We have also attempted to fit the SAXS data with stacking of disks as parallel arrays of lamellar crystals in the traditional view, using the disk form factor and the arrayed-lamellae structure factor[42] expressed $S_{AL} = N + 2\Sigma_{k=1}^{N-1}(N-k)\cos(kqL)\exp(-k^2q^2\Delta^2/2)$, where N is the number of stacked layers and Δ the root-mean-squared fluctuations of long period L. As shown in Figure 6, the fitting curves obtained deviate significantly from the data for $q > 0.07$ Å^{-1}, in dramatic contrast to Figure 2c using a combination of ellipsoidal form and hard-sphere structure factors. This alternative (and more traditional) model of stacked disks may thus be safely excluded. Incidentally, the fitted number of layers is around 2 for all curves in Figure 6 (cf. Supporting Information), implying very limited order in spatial arrangement of the nanograins and hence reaffirming the picture of disordered FCC-like packing.

Concomitant with the increase in nanograin size revealed via SAXS, gradual sharpening of (110), (300), (220), and (211) reflections of α crystals is observed in WAXS profiles given in Figures 3a and 4a; this is more clearly illustrated by the evolution of the crystallite dimensions (calculated from the reflection peak widths using the Scherrer equation) in Figure 4b. These crystallite dimensions match closely with the nanograin envelopes extracted with SAXS (cf. Figure 5a).

The increase in nanograin size concomitant with the expansion of intergrain spacing in this temperature range cannot be attributed to a straightforward growth of individual nanograins without interactions, as there are also no corresponding thermal events (Figure 3b). With little alternative, such behavior directs to the mechanism of coalescence of neighboring nanograins through rotation and attachment, as previously proposed for nanocrystals[43] in general and PFO nanograins[20] in particular. In view of the preference of polymers to form lamellar crystals, it is only natural to assume that sPS chains are oriented along the major (short) axis of the oblate ellipsoids. Coalescence would then be achieved via aligning the major oblate axis through thermally activated rotation of neighboring nanograins, in agreement with the preferred size increase within the crystallographic $a \times b$ plane (cf. Figure 4b).

Plausibility of the proposed rotation-attachment process is manifested by the observation that, shortly (ca. 1 min) after reaching 240 °C for isothermal annealing, there are little further changes in both SAXS and WAXS profiles, indicating quick completion of the coalescence-thickening process at a given temperature. The process is characteristically different from the classic (and much slower) case of lamellar thickening during long-term isothermal annealing at an elevated temperature. As previously proposed,[8,43] attachment and coalescence of nanocrystals require nanograin alignment via thermally activated fluctuations of neighboring nanocrystals. Proceeding of coalescence results in network strains from entangled chains in the immediate surrounding of the nanograin multiply connected to the surrounding matrix; consequently, the quickly reached quasi-equilibrium with the matrix forbids further coalescence with other neighboring nanograins. In other words, the final morphology corresponds to coalesced nanograins with the size determined by the final temperature of the cold crystallization process. It follows that there should be a maximum temperature at which the free energy gain from coalescence/thickening can no longer support the coalescence. Attempt to identify such an upper limit is currently in progress; results are to be reported in the near future.

Scenario of Structural Evolution. Figure 5 summarizes the structural information revealed by in-situ SAXS/WAXS/DSC for the cold crystallization process of sPS. Before T_1 (≈90 °C) is the eventless frozen-in stage and hence trivial. Between T_1 and T_2 (≈130 °C) is the nucleation stage, where oblate-like nuclei of similar size emerge and increase in number; concurrently, the emergence of the scattering invariant Q_{inv} reflects the increased degree of heterogeneity due to the formation of nanograins (Figure 5b). In the growth stage between T_2 and T_3 (≈180 °C), nanograins (of fixed concentration n_p and center-to-center spacing d) grow significantly with decreased shape anisotropy (cf. Figure 5a, the smaller B/A ratio than that in the nucleation stage) and develop into distorted-FCC-like arrangement, resulting in extensively developed heterogeneity and hence rapidly increased Q_{inv} (Figure 5b). Thermal events concerning cold crystallization are essentially completed at the end of this stage as revealed by DSC (Figure 3b), although WAXS results (Figures 3a and 4) indicate an ongoing development in the long-range positional order (Figure 5b).

Above T_3 is the coalescence stage, where the nanograins grow by coalescence, resulting in a rapid increase in size, especially along the plane of minor oblate axis. This leads to

Downloaded by SYNCHROTRON RADIATION RES CTR on September 1, 2009 | http://pubs.acs.org
Publication Date (Web): June 25, 2009 | doi: 10.1021/ma900537c

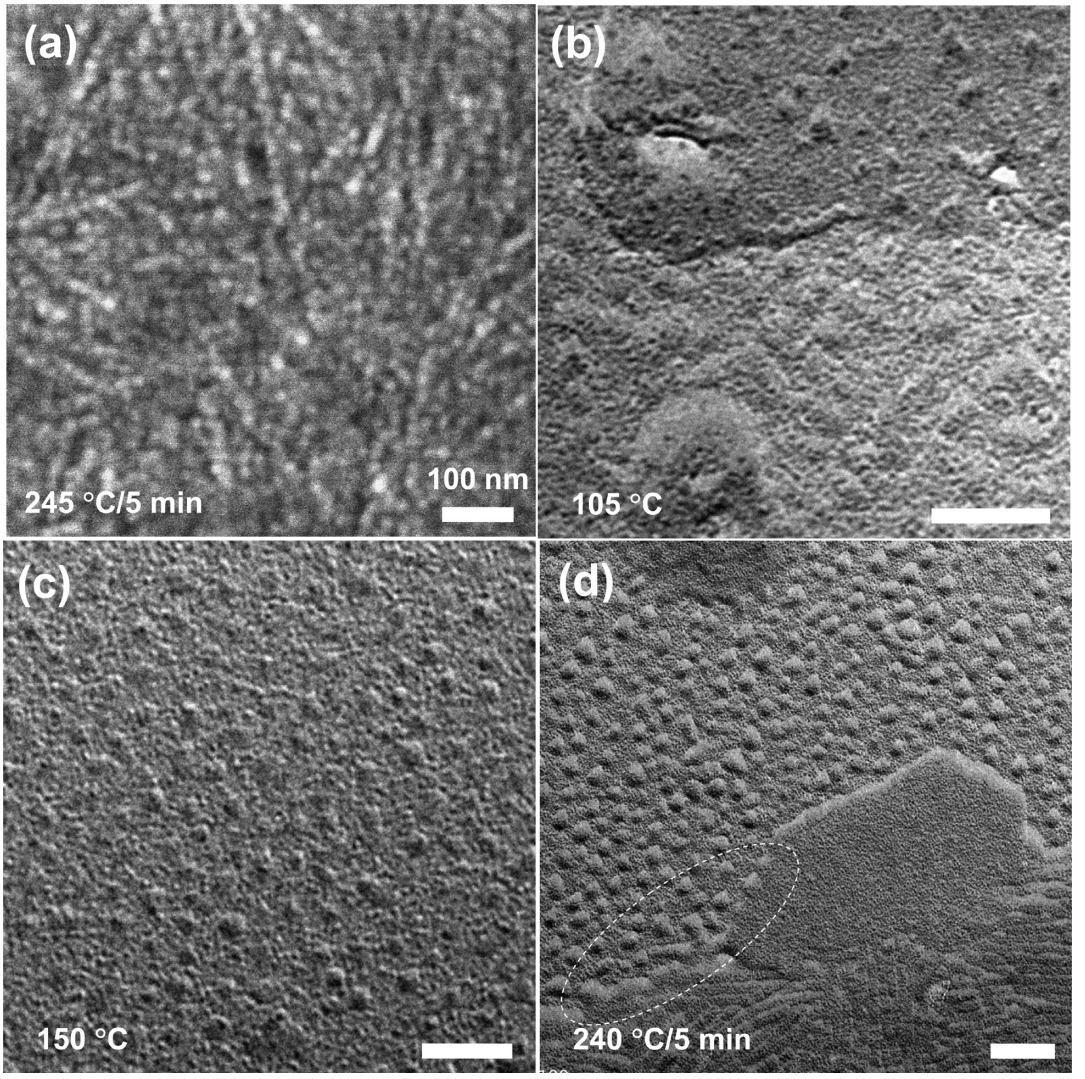

Figure 7. (a) Representative SEI of a quenched sPS film after cold crystallization at 245 °C for 5 min. Bright nodules (2-D projected as 10−15 nm in size and 18−20 nm in center-to-center internodular spacing) are clearly identifiable and consistent with the SAXS-derived model of sPS nanograins as oblate ellipsoids ($2A \approx 8$ nm, $2B \approx 14$ nm) with a mean center-to-center spacing $d \approx 17$ nm. Note the tendency of nanograins to loosely attach (without coalescence) into fibrils. Also shown are representative BFI of thin-film specimen (Pt/C shadowed at 60° from film normal) of the same thermal history as the SAXS/WAXS specimen (b) at 105 °C, (c) at 150 °C, and (d) maintained isothermal at the maximum temperature of 240 °C for 5 min before quenching into ice water. As the contrast is mainly due to Pt shadowing, the light shadow should be corrected by a factor of sin 30° for height where as the dark region corresponds to part of nodule facing the Pt source. As both particle shape and orientation affect the image, there are some uncertainties in the estimated size of ca. 5 nm in the upper part of (b); the lower part of the view is of low surface roughness (probably due to lower nuclear density) and hence comparatively featureless. Nodules in (c) are more easily identifiable and appear comparable to or slightly larger than 5 nm. Isolated nanograins ca. 10−15 nm in size (with hints of coalescence for larger nanograins) are clearly seen in the upper-left half of (d). In the lower right half of the view, densely nucleated nanograins have further coalesced into edge-on (bottom) or flat-on (central right) lamellae ca. 10 nm in thickness. The encircled region highlights the coalescence process in progress. In contrast to thick-film/bulk specimens, the quasi-2-D environment (and hence easier orientation of nanograins)[45] in cold crystallized sPS thin films tends to enhance the lateral attachment of nanograins into fibrils and even flat-on single crystals. Scale bars correspond to 100 nm.

Downloaded by SYNCHROTRON RADIATION RES CTR on September 1, 2009 | http://pubs.acs.org
Publication Date (Web): June 25, 2009 | doi: 10.1021/ma900537c

extensively developed lateral dimension up to 14 nm (in terms of the minor axis $2B$), with some concomitant ordering and lamellar thickening along the chain axis up to ca. 7 nm (in terms of the major axis $2A$), as given in Figure 5a. This coalescence process does not involve significant changes in the degree of heterogeneity Q_{inv} as compared to the growth stage (Figure 5b); nor does it involve any discernible thermal event (Figure 3b). On the other hand, the crystallinity $X_{c,WAXS}$ extracted from the WAXS profiles is still strongly increasing in this stage (Figure 4b), with intensified/sharpened ($hk0$) reflections. These results indicate a drastic improvement in the long-range positional order transverse to the molecular axis that is consistent with the steadily increasing lateral size up to 14 nm at 240 °C (Figure 5a). The dynamic process is temperature-dependent and essentially instantaneous (within the time scale of 1 min); further annealing at 240 °C results in no discernible changes.

Discussion

Nanograin Images in Real Space. All structural features discussed above correspond to scattering results in reciprocal space. It is of interest to compare the model with microscopic observations in real space. Figure 7a exhibits a representative secondary electron image (SEI) of a thick sPS film quenched upon cold crystallization at 245 °C for 5 min, where nanograins are clearly identifiable. The particle size and the center-to-center spacing are consistent with those revealed from the SAXS results upon due corrections for the 2-D plan

Downloaded by SYNCHROTRON RADIATION RES CTR on September 1, 2009 | http://pubs.acs.org
Publication Date (Web): June 25, 2009 | doi: 10.1021/ma900537c

view. There are also fibrillar features reminiscent of primitive spherulites in the micrometer scale, which correspond to higher order aggregates beyond our SAXS low-q limit and have in fact been better resolved via light scattering (LS) by Wang et al.[44] with accompanying bright-field images (BFI) of micotomed/RuO_4-stained specimens of sPS cold crystallized in bulk. It is then interesting to note that, although Wang et al. have adopted the traditional view of lamellar growth in spherulites to interpret their LS results, the supplementary BFI (Figure 12 therein)[44] indeed demonstrated the presence of isolated nanograins as well as fibrils of aligned nanograins, both features are in excellent agreement with those exhibited in Figure 7a. All these observations are consistent with the proposed model that oblate nanograins serve as units of morphological development during the away-from-equilibrium process of cold crystallization.

Shown in Figure 7b−d are representative BFI of thin-film specimens of the same thermal history as the SAXS/WAXS/DSC specimen before quenching into ice water. Care must be exercised in interpreting the shadowed 2-D images of these quasi-2-D specimens detached from glass substrates;[4] there exist intrinsic differences from the essentially 3-D case of SAXS/WAXS specimens. In Figure 7b,c, small nodules having apparent dimensions of 5−10 nm at 105 and 150 °C correspond to the nanograins in respective nucleation and growth stages revealed by SAXS (cf. Figure 5a). In Figure 7d, isolated nanograins of larger sizes (10−15 nm) can be identified in the thinner region (upper-left half of the view) of low areal nuclear density. With increasing areal density of nuclei, there are flat-on single crystals (lower right) and edge-on lamellae (bottom) ca. 10 nm in crystal thickness. There are also clear features of merging nanograins at developing front of the single crystal and at the boundary zone between regions of stacked edge-on lamellae and isolated nanograins. In other words, the quasi-2-D environment (and hence easier orientation of nanograins)[45] in cold crystallized sPS thin films tends to enhance the lateral attachment of nanograins into fibrils and even flat-on single crystals. This is consistent with the ease of obtaining single crystals via melt crystallization of thin films,[4,46−48] in contrast to the traditional view that single crystals are supposedly limited to crystallization from dilute solutions.

Nuclear Size and Chain Rigidity. Reminiscent of the fringed-micelle model[49] for nanometer-sized crystallites and the more recent bundle model[50] for molecular nucleation, we have proposed in the previous case of PFO that nucleation during cold crystallization corresponds to laterally aggregated stems with the molecular axis oriented along the major axis. As stems aggregate, the entangled chains in the immediate neighborhood are expected to become more tightly locked: only limited reptational displacement is expected in view of the low mobility of chains at temperatures only modestly higher than T_g. Such behavior not only sets a natural limit to the nuclear size/shape but also excludes further nucleation in the "knotted" vicinity of an existing nucleus. The latter results in subsequent nucleation at sites midway between neighboring nuclei and hence the distorted FCC-like structure at the end of the nucleation stage, yielding a clearly emerged SAXS peak at the end of the nucleation stage.

The nucleation scenario appears applicable to the present case of sPS (cf. Figures 2 and 5) as well. The nuclear size and shape, however, differ characteristically from that of PFO, originating presumably to the differences in chain characteristics between the two polymers. The nuclei of PFO ($A \approx$ 6.4 nm, $B \approx$ 2.4 nm, and $R_g \approx$ 3.3 nm) are prolate in shape and generally greater in size as compared to the oblate nuclei in sPS ($A \approx$ 1.3 nm, $B \approx$ 4.0 nm, and $R_g \approx$ 2.6 nm). Values of the shorter principal axis compare reasonably with corresponding values of the persistence length ($l_{p,sPS} \approx$ 1.9 nm and $l_{p,PFO} \approx$ 8.6 nm).[51−53] The greater lateral dimension of sPS nuclei is attributed to the higher flexibility (and hence stronger tendency to fold back and re-enter the nucleus) of sPS as compared to PFO backbones. The lower value of the nuclear volume ($V = 4\pi AB^2/3 = 20.8$ nm^3) for sPS in contrast to the case of PFO (37.4 nm^3) may have several contributing factors such as free energy of crystallization, basal plane surface energy, and elasticity of entangled chains, but a major role should be played by the finer entanglement mesh size and hence more limited contour length (L_e) between entanglement points for this just-devitrified nucleation stage devoid of effective reptation. According to Wu,[54] the number of rotating bonds between entanglements can be related to the characteristic ratio as $N_e = 3C_\infty^2$. With $C_{\infty,PFO} \approx 36$ and $C_{\infty,sPS} \approx 10$,[54,55] the contour length between entanglements may be estimated as $L_{e,PFO} \approx 0.836$ nm $\times 3 \times 36^2 = 3250$ nm and $L_{e,sPS} = 0.154$ nm $\times 3 \times 10^2 = 46.2$ nm. This difference by nearly 2 orders of magnitude is expected to outweigh other contributing factors.

Growth Limited by Number Density of Nanograins. The growth stage is characterized by the increase of nanograin size upon saturated nucleation into a relatively constant (micelle-like, distorted FCC) lattice structure (i.e., fixed SAXS peak position; cf. Figure 2b) and the accompanying appearance of crystalline reflections in WAXS (Figures 3a and 4a). This may be explained in terms of increased chain mobility with temperature, which results in relaxed knots and hence growth of nuclei into nanocrystals of identifiable WAXS reflections in the growth stage.

It is then illuminating to note that the size growth in sPS nanograins (from $R_g \approx$ 2.6 nm at 90 °C to $R_g \approx$ 3.1 nm at 130 °C) is rather modest as compared to that in the growth regime of PFO cold crystallization (from $R_g \approx$ 3.3 nm at 90 °C to $R_g \approx$ 5.0 nm at 110 °C). The more limited growth is directly related to the smaller nuclear size and the larger number density of the sPS nuclei (i.e., smaller intergrain spacing) at the end of nucleation stage; the mean intergrain spacing $d \approx$ 13 nm at the end of nucleation stage is much shorter than that in the case of PFO ($d \approx$ 24 nm). As the coalescence stage would start at the contact of nanograins, the shorter d value sets a natural limit to the end of growth stage as the dimension transverse to chain direction ($2A$ in the case of prolate ellipsoids in PFO and $2B$ in the present case of sPS) approaches d. For PFO, the transition from growth to coalescence occurred at $2A$ = 20 nm; for sPS, at $2B$ = 9 nm. In view of local fluctuations in nanograin positions, such a kind of transition is unlikely to be sharp and hence started somewhat below the corresponding d values.

Coalescence Opposed by Matrix Chain Entanglement. Coalescence of neighboring nanograins leads to the increased nanograin spacing, as revealed by the characteristic low-q shift of the SAXS peak in Figure 2c. As proposed previously, coalescence of neighboring nanograins involves orientated attachment via thermal fluctuations. At a given temperature, the final coalesced nanocrystallites are kinetically trapped to a size at which the thermal energy can no longer provide sufficient rotational freedom for nanograin alignment, as demonstrated by the absence of changes in SAXS/WAXS/DSC traces under isothermal annealing once a maximum temperature (240 °C here for sPS and 145 °C in the previous case of PFO) is reached.

Countering the thermally activated rotation in the process is the elastic force from the melt matrix of knotted/tightened

chains. In the case of PFO, this effect is weak in view of the low entanglement density directly; the nematic nature of the melt state is also advantageous for coalescence, as chains in the melt and hence nanograins nucleated are largely aligned. Compared to PFO, sPS melt is isotropic and highly entangled, resulting in stronger resistance toward nanograin rotation in spite of the higher experimental temperatures (up to 240 °C, as compared to 145 °C in the previous case of PFO). Consequently, sPS nanograins coalesce modestly with R_g increasing from 3.2 nm (at 180 °C) to 4.6 nm (at 240 °C), as contrasted by $R_g \approx 5$ nm (at ca. 110 °C) to 10 nm (at 145 °C) for PFO. In other words, the higher entanglement density in the present case of random-coiled sPS chains results in not only the smaller nuclear size but also the more limited final size upon nanograin coalescence as compared to rigid PFO chains.

Conclusions

In terms of nucleation, growth, and coalescence of nanograins, proposed previously for the cold crystallization of PFO based on SEM and TEM images and SAXS/WAXS/DSC results, we have demonstrated here that a similar nanograin evolution process explains the observed density fluctuations during cold crystallization of random-coiled sPS chains. It appears that the persistence length (and hence the contour length between entanglements) determines the size/shape of nanograins in cold crystallization: the shorter persistence length (and hence the higher entanglement density) of sPS results in smaller nuclei (that are oblate in shape), more limited growth, and relatively modest extent of nanograin coalescence as compared to the previous case of semirigid PFO chains.

Acknowledgment. Financial support from the National Science Council (Grants NSC96-2221-E-007-015 and NSC96-2112-M-213-008-MY3) is gratefully acknowledged. Helpful discussions with Dr. T.-L. Lin are acknowledged.

Supporting Information Available: Comparison with traditional models of disks or stacked lamellae. This material is available free of charge via the Internet at http://pubs.acs.org.

References and Notes

(1) Chen, S. H.; Su, A. C.; Chou, H. L.; Peng, K. Y.; Chen, S. A. *Macromolecules* **2004**, *37*, 167.
(2) Chen, S. H.; Su, A. C.; Han, S. R.; Chen, S. A.; Lee, Y. Z. *Macromolecules* **2004**, *37*, 181.
(3) Chen, S. H.; Su, C. H.; Su, A. C.; Chen, S. A. *J. Phys. Chem. B* **2004**, *108*, 8855.
(4) Chen, S. H.; Chou, H. L.; Su, A. C.; Chen, S. A. *Macromolecules* **2004**, *37*, 6833.
(5) Jeng, U.; Hsu, C. H.; Sheu, H. S.; Lee, H. Y.; Inigo, A. R.; Chiu, H. C.; Fann, W. S.; Chen, S. H.; Su, A. C.; Lin, T. L.; Peng, K. Y.; Chen, S. A. *Macromolecules* **2005**, *38*, 6566.
(6) Chen, S. H.; Su, A. C.; Chen, S. A. *J. Phys. Chem. B* **2005**, *109*, 10067.
(7) Chen, S. H.; Su, A. C.; Chen, S. A. *Macromolecules* **2006**, *39*, 9143.
(8) Chen, S. H.; Wu, Y. H.; Su, C. H.; Jeng, U.; Hsieh, C. C.; Su, A. C.; Chen, S. A. *Macromolecules* **2007**, *40*, 5353.
(9) Kaji, K.; Nishida, K.; Kanaya, T.; Matsuba, G.; Konishi, T.; Imai, M. *Adv. Polym. Sci.* **2005**, *191*, 187 and references cited therein.
(10) Schultz, J. M.; Lin, J. S.; Hendricks, R. W.; Petermann, J.; Gohil, R. M. *J. Polym. Sci., Polym. Phys.* **1981**, *19*, 609.
(11) Heeley, E. L.; Poh, C. K.; Li, W.; Maidens, A.; Bras, W.; Dolbnya, I. P.; Gleeson, A. J.; Terrill, N. J.; Fairclough, J. P. A.; Olmsted, P. D.; Ristic, R. I.; Hounslow, M. J.; Ryan, A. J. *Faraday Discuss.* **2002**, *122*, 343.
(12) Wang, Z.-G.; Hsiao, B. S.; Sirota, E. B.; Srinivas, S. *Polymer* **2000**, *41*, 8825.
(13) Fougnies, C.; Damman, P.; Villers, D.; Dosiere, M.; Koch, M. H. J. *Macromolecules* **1997**, *30*, 1385–1391.
(14) Mano, J. F.; Wang, Y.; Viana, J. C.; Denchev, Z.; Oliveira, M. J. *Macromol. Mater. Eng.* **2004**, *289*, 910.
(15) Terrill, N. J.; Fairclough, P. A.; Towns-Andrews, E.; Komanschek, B. U.; Young, R. J.; Ryan, A. J. *Polymer* **1998**, *39*, 2381.
(16) Imai, M.; Kaji, K.; Kanaya, T. *Phys. Rev. Lett.* **1993**, *71*, 4162.
(17) Penn, R. L. *J. Phys. Chem. B* **2004**, *108*, 12707.
(18) Strobl, G. *Eur. Phys. J. E* **2000**, *3*, 165.
(19) Ryan, A. J.; Fairclough, J. P. A.; Terrill, N. J.; Olmsted, P. D.; Poon, W. C. K. *Faraday Discuss.* **1999**, *112*, 13.
(20) Su, C. H.; Jeng, U.; Chen, S. H.; Lin, S. J.; Ou, Y. T.; Chuang, W. T.; Su, A. C. *Macromolecules* **2008**, *41*, 7630.
(21) Konishi, T.; Nishida, K.; Kanaya, T. *Macromolecules* **2006**, *39*, 8035.
(22) Peterlin, A. *Text. Res. J.* **1972**, *42*, 20.
(23) Chen, Y. P.; Tsai, J. C.; Hong, J. L. *J. Chin. Chem. Soc.* **2003**, *50*, 205.
(24) Lai, Y. H.; Sun, Y. S.; Jeng, U.; Lin, J. M.; Lin, T. L.; Sheu, H. S.; Chuang, W. T.; Huang, Y. S.; Hsu, C. H.; Lee, M. T.; Lee, H. Y.; Liang, K. S.; Gabriel, A.; Koch, M. H. J. *J. Appl. Crystallogr.* **2006**, *39*, 871.
(25) Chen, S. H.; Lin, T. L. In *Methods of Experimental Physics - Neutron Scattering in Condensed Matter Research*; Sköld, K., Price, D. L., Eds.; Academic: New York, 1987; Vol. *23B*, Chapter 16.
(26) Feigin, L. A.; Svergun, D. I. *Structure Analysis by Small-Angle X-ray and Neutron Scattering*; Plenum: New York, 1987; p 69.
(27) Baxter, R. J. *J. Chem. Phys.* **1970**, *52*, 4559.
(28) Pedersen, J. S. *J. Appl. Crystallogr.* **1994**, *27*, 595.
(29) Tsao, C.-S.; Lin, T.-L.; Yu, M.-S. *Physica B* **1999**, *271*, 322.
(30) Krakovasky, I.; Urakawa, H.; Kajiwara, K. *Polymer* **1997**, *14*, 3645.
(31) Chen, S. H.; Sheu, E. Y.; Kalus, J.; Hoffmann, H. *J. Appl. Crystallogr.* **1988**, *21*, 751.
(32) Chuang, W.-T.; Jeng, U.; Sheu, H.-S.; Hong, P.-D. *Macromol. Res.* **2006**, *14*, 45.
(33) Su, C. H.; Jeng, U.; Chen, S. H.; Cheng, C.-Y.; Lee, J.-J.; Lai, Y.-H.; Su, W. C.; Tsai, J. C.; Su, A. C. *Macromolecules* **2009**, *42*, 4200, and references cited therein.
(34) Freltoft, T.; Kjems, J. K.; Sinha, S. K. *Phys. Rev. B* **1986**, *33*, 269.
(35) Teixeira, J. *J. Appl. Crystallogr.* **1988**, *21*, 781.
(36) Schmidt, P. *J. Appl. Crystallogr.* **1991**, *24*, 414.
(37) Higgins, J. S.; Benoit, H. C. *Polymer and Neutron Scattering*; Oxford University Press: New York, 1994; p 174.
(38) Sheu, E. Y. *Phys. Rev. A* **1992**, *45*, 2428.
(39) Jeng, U.; Liu, W.-J.; Lin, T.-L.; Wang, L. Y.; Chiang, L. Y. *Fullerene Sci. Technol.* **1999**, *7*, 599.
(40) Huang, Y.-Y.; Hsu, J.-Y.; Chen, H.-L.; Hashimoto, T. *Macromolecules* **2007**, *40*, 406.
(41) Cartier, L.; Okihara, T.; Lotz, B. *Macromolecules* **1998**, *31*, 3303.
(42) Richter, D.; Schneiders, D.; Monkenbusch, M.; Willner, L.; Fetters, L. J.; Huang, J. S.; Lin, M.; Mortensen, K.; Fargo, B. *Macromolecules* **1997**, *30*, 1053.
(43) Shen, P.; Fahn, Y. Y.; Su, A. C. *Nano Lett.* **2001**, *1*, 299 and references cited therein.
(44) Wang, C.; Lin, C. C.; Chu, C. P. *Polymer* **2005**, *46*, 12595.
(45) Masson, A.; Métois, J. J.; Kern, R. *Surf. Sci.* **1971**, *27*, 463.
(46) Lotz, B.; Lovinger, A. J.; Cais, R. E. *Macromolecules* **1988**, *21*, 2375.
(47) Bu, Z.; Yoon, Y.; Ho, R. M.; Zhou, W.; Jangchud, I.; Ebby, R. K.; Cheng, S. Z. D.; Hsieh, E. T.; Johnson, T. W.; Geerts, R. G.; Palackal, S. J.; Hawley, G. R.; Welch, M. B. *Macromolecules* **1996**, *29*, 6575.
(48) Ho, R. M.; Lin, C. P.; Hseih, P. Y.; Chung, T. M.; Tsai, H. Y. *Macromolecules* **2001**, *34*, 6727.
(49) Geil, P. H. *Polymer Single Crystals*; Wiley: New York, 1973; pp 7−10.
(50) Allegra, G.; Meille, S. V. *Adv. Polym. Sci.* **2005**, *191*, 87.
(51) Matsuba, G.; Kaji, K.; Nishida, K.; Kanaya, T.; Imai, M. *ICR Ann. Rep.* **1999**, *6*, 26.
(52) Grell, M.; Bradley, D. D. C.; Long, X.; Chamberlain, T.; Inbasekaran, M.; Woo, E. P.; Soliman, M. *Acta Polym.* **1998**, *49*, 439.
(53) Tsoi, W. C.; Charas, A.; Cadby, A. J.; Khalil, G.; Adawi, A. M.; Iraqi, A.; Hunt, B.; Morgado, J.; Lidzey, D. G. *Adv. Funct. Mater.* **2008**, *18*, 600.
(54) Wu, S. *Polym. Eng. Sci.* **1992**, *32*, 823.
(55) Stölken, S.; Ewen, B.; Kobayashi, M.; Nakaoki, T. *J. Polym. Sci., Polym. Phys.* **1994**, *32*, 881.

Downloaded by SYNCHROTRON RADIATION RES CTR on September 1, 2009 | http://pubs.acs.org
Publication Date (Web): June 25, 2009 | doi: 10.1021/ma900537c